# On the use of nanoscale multilayers to determine interdiffusion coefficients: comprehensive characterization of interdiffusion at low temperature in the Ni-Cr system

T Rieger, M. Nastar, Aurelien Debelle, Anny Michel, Alain Billard, Marie Loyer-Prost

# On the use of nanometer-scale multilayers to determine interdiffusion coefficients: comprehensive characterization of interdiffusion at low temperature in the Ni–Cr system

T. Rieger[a], M. Nastar[a], A. Debelle[a,b], A. Michel[c], A. Billard[d], M. Loyer-Prost[a,*]

[a] *Université Paris-Saclay, CEA, Service de recherche en Corrosion et Comportement des Matériaux, SRMP, F-91191, Gif-sur-Yvette, France*
[b] *Université Paris–Saclay, CNRS/IN2P3, IJCLab, F-91405, Orsay, France*
[c] *Institut PPrime, UPR 3346, Université de Poitiers-CNRS-ENSMA, F-86960, Chasseneuil-Futuroscope, France*
[d] *FEMTO-ST, UMR 6174 CNRS, MN2S Department, Univ. Bourgogne Franche-Comté, UTBM, Rue Thierry Mieg, F-90000, Belfort, France*

**Abstract**

Nanoscale multilayers are a convenient way to determine interdiffusion coefficients at low temperatures. However, knowledge on the impact of the microstructure on measurements is limited. In the present study, we measure the interdiffusion coefficient in the face-centered cubic (fcc) solid solution of the Ni–Cr system at 440°C using multilayers consisting of alternating layers of pure Ni and Ni20Cr (wt.%), with a nominal wavelength of 4.5 nm. Three techniques were used to characterize the evolution of the multilayers with annealing: atom probe tomography (APT), energy-dispersive X-ray spectroscopy (STEM-EDX) and X-Ray reflectivity (XRR). Each of the three techniques allowed to determine an interdiffusion coefficient. The results evidence that the interdiffusion coefficient is dependent from the technique used to measure it. The primary cause is a very complex microstructure resulting from the elaboration method used to obtain the fine concentration modulation. The analysis of atom probe tomography volumes reveals a high density of columnar grain boundaries (GB) with extended chemical widths. The segregation at GB was measured and a model was derived, allowing to dissociate the contribution of diffusion along and perpendicularly to GBs. The present results could serve as guides for future diffusion investigations involving multilayers.

*Keywords:* Diffusion, Atom Probe Tomography, Energy-Dispersive X-ray Spectroscopy, X-ray Reflectivity, Multilayers

## 1. Introduction

Chemical diffusion is a key phenomenon, responsible for microstructural evolutions in metallic alloys occuring during processing and in service, such as phase transitions, oxidation [1], growth [2] and coarsening

*Corresponding author
*Email address:* marie.loyer-prost@cea.fr (M. Loyer-Prost)

[3] of precipitates that can lead to major changes in properties. Diffusion data are thus crucial to predict the lifetime of critical components during service. In the case of low temperatures (typically below 600°C), lattice diffusion can be challenging to characterize due to a combination of small diffusion lengths even after extended annealing times and a predominance of diffusion along high-diffusivity paths, such as grain boundaries (GB). First introduced by DuMond and Youtz in 1939 [4], nanoscale multilayers are an easy way to access very small diffusion lengths with good accuracy. The decay of the electronic density modulation introduced by the stacking of layers with different chemical compositions can be monitored with the help of X-ray reflectivity (XRR). Moreover, additional thermodynamic and kinetic information can be extracted from such measurements. It is expected that the diffusion coefficient becomes dependent on the wavelength of chemical concentration modulation at small enough values due to the impact of interface-related gradient energy [5–7] and kinetic correlation effects [8]. This method has since been used to access previously unreachable ranges of self-diffusion [9] and interdiffusion coefficients in multiple binary [10–14] and ternary systems [15]. However, the methods used to synthesize the multilayers usually result in highly-disturbed microstructures with a high density of defects such as GBs and/or dislocations [16]. It is well established that the quality of diffusion measurements depends on the method used and the extent to which the sample material is characterized [17]. Since the interdiffusion coefficient is usually determined by means of macroscopic diffusion experiments with indirect measurements of the amplitude mitigation (XRR or XRD) and rarely accompanied by fine microstructure characterizations, knowledge on the impact of microstructural features on measurements of interdiffusion coefficients is limited.

Interdiffusion coefficients were recently determined in the face-centered cubic (fcc) solid solution of the Ni–Cr system with the help of Ni-Ni20Cr (wt.%) multilayers at 400°C and 450°C ($7.7 \times 10^{-25}$ m$^2$/s and $7.1 \times 10^{-24}$ m$^2$/s, respectively) using X-ray reflectivity (XRR) [18, 19]. The main finding is that the interdiffusion coefficient is independent from the concentration modulation wavelength in the interval between 3.6 and 4.5 nm, within experimental errors. Two distinct regimes were observed, with a transient first regime during which a significant decrease in intensity was evidenced. This decrease was tentatively attributed to diffusion in short-circuit diffusion paths during the first stages of annealing. A similar yet less pronounced transient was already observed in Au–Ag multilayers by Cook and Hilliard [10]. The authors attributed this phenomenon to an enhanced diffusivity during grain growth or recrystallization. In any case, it is not clear whether this phenomenon is only restricted to the first transient or if it also contributes to the further evolution of the signal. A review conducted by Zotov and Ludwig on interdiffusion coefficients measured with multilayers tend to confirm that global measurements should be treated with caution [20].

Many questions remain unanswered regarding the Ni–Cr system but also from a more comprehensive perspective, on the use of multilayers for the determination of interdiffusion coefficients: (1) what is the origin of the first transient observed with XRR? (2) Can it influence measurements in the second regime, which is

usually used for the determination of the interdiffusion coefficient? (3) If so, does it have a significant impact and can it be corrected? This last question brings to a more global question: to what extent are global characterization methods (such as XRR and XRD) suitable for the measurement of interdiffusion coefficients in multilayers? (4) What are the limitations of multilayers for interdiffusion as a function of temperature, wavelength and microstructural features? To adress these questions, three characterization methods are used to determine the interdiffusion coefficient in Ni-Ni20Cr multilayers: atom probe tomography (APT), probe-corrected energy-dispersive X-ray spectroscopy (STEM-EDX) and XRR. The particular interest of the combination of these three techniques is that they offer a wide range of probed volumes, XRR being the most commonly used and also the most global. APT is the most local technique, to a point that it can theoretically allow to avoid the influence of GBs in multilayers with nanometer-scale grain sizes. The samples from reference [18], with a nominal wavelength $\Lambda = 4.5$ nm annealed at 450°C and already characterized with XRR were chosen to conduct this study.

## 2. Methods

### *2.1. Deposition, annealing of samples and XRR*

The multilayers were prepared by magnetron sputtering with a nominal wavelength $\Lambda = 4.5$ nm, following a procedure described elsewhere [18]. Prior to deposition of the layers, a first layer of SiNx or SiOx was deposited onto the Si substrate to act as a diffusion barrier. The portion of interest is composed of a first part of alternating layers of Ni and Ni20Cr ($\sim$ 550 nm) followed by a large layer of pure Ni ($\sim$ 80 nm), after which the alternating layers continue up to the surface ($\sim$ 250 nm). The Ni layer between the multilayers (which will be later referred to as the large Ni layer) remained previously unexploited using XRR since it is too deep for the signal to reach it. The samples were annealed in a tubular furnace under vacuum ($10^{-4}$ Pa) at a setpoint of 450°C. In light of recent measurements, the temperature inside the furnace is estimated to be 10°C lower than the targeted one (440°C). XRR measurements were then performed using a 4-circle Seifert XRD3000 diffractometer with a Cu K$\alpha$ source. For more details on the deposition technique and the XRR measurements, the reader is referred to reference [18].

### *2.2. STEM-EDX*

Scanning Transmission Electron Microscopy observations (STEM) and subsequent EDX chemical characterizations were performed using a Jeol NEOARM operated at 200 kV and equipped with a probe corrector and the JED Analysis Station software. The samples for both STEM-EDX and APT observations were prepared by FIB (Focused Ion Beam) milling using a FEI Helio 650 NanoLab dual-beam scanning electron microscope. For STEM-EDX analysis, the thin foil is oriented with the help of the [111] zone axis of the Si substrate which is normal to the deposition direction. A EDX map is measured in a 40x40 nm$^2$ area in which a 10 nm wide profile is extracted following map quantification. This procedure allows the selection

of a profile in area distanced from GBs and the obtention of a quantitative profile (more than 10k counts per measurement point). The given grain size was determined using a top view of the multilayers and is the diameter of a disk with equivalent surface area.

For both STEM-EDX and APT profiles, the amplitude is extracted from a sine fit of experimental data considering only Cr and Ni contributions. The given amplitude values are the mean of all measurements. All given uncertainties are a 95% confidence interval, assuming a normal distribution of measurements.

### *2.3. Atom Probe Tomography*

#### *2.3.1. Analysis conditions and reconstruction*

Atom Probe Tomography (APT) analysis was performed using a CAMECA LEAP 4000XHR device at a set point temperature of 50K in laser pulsing mode with a 20 pJ laser energy at a wavelength of 382 nm and a 200 kHz pulse repetition rate. As many as 5 different samples were analyzed for each condition to ensure adequate statistics. The reconstruction was performed with the commercially available IVAS software. The existence of a difference in evaporation field between Ni and Ni20Cr prohibits the use of a voltage reconstruction, it was thus carried out in shank mode and consistently calibrated in scale by finding a (111) pole and by adjusting the parameters to obtain the corresponding interatomic distance in the whole sequence of evaporation. The overall chemical composition was determined with a isotopic decomposition of peaks and a decomposition of complex ions.

#### *2.3.2. GBs*

The GBs were identified thanks to their high oxygen content. As a result, some of the atoms are ionized as complex ions, such as CrO or NiO, which act as markers that differentiate them from crystallographic poles. Grain size was measured on reconstructed volumes using upper views of CrO ions in clipped sections. The given grain size is the diameter of a disk with equivalent surface area. These measurements must be taken with caution since they depend on the lateral resolution of APT reconstructions.

#### *2.3.3. Local method of amplitude determination*

Two methods were applied to the reconstructed volumes in order to extract a Cr modulation amplitude. In the first, referred to as the local method, a cylinder of 10 nm in diameter and 30 nm in height is extracted from the main volume as far as possible from GBs. Chemical concentration profiles are generated from sub-volumes (roughly 2 to 3 for a volume of 5 million ions), which are extracted manually for each volume. This method is not time-efficient since it requires special care to select sub-volumes oriented perpendicularly to the layers that are not influenced by GBs.

#### *2.3.4. Global method of amplitude determination*

The second method is referred to as the global method and aims at analyzing the whole volume at once. After reconstruction, the APT volume is voxelised with a given box size. After careful removal of the edges

of the volume, a distribution histogram of Cr concentration inside the volume is generated. The choice of the box size is critical and constitutes a trade-off between spatial resolution and statistics. A parameter analysis highlighted that the ideal trade-off for the studied wavelength ($\Lambda$ = 4.5 nm) is obtained for a box size of 1×1×1 nm$^3$ which corresponds to an average of 39 atoms of Cr and Ni inside each box. In order to obtain a smooth distribution, a delocalization algorithm is applied to the voxels in the directions perpendicular to the deposition direction. The resulting distribution contains all the information needed to retrieve the concentration modulation amplitude. However, the statistical nature of APT data and the presence of GBs require a thorough analysis to avoid any error.

First, a statistical analysis is carried out: the atoms inside the initial volume are randomly labeled with a varying Cr concentration (from 2 at.% to 22 at.% with a 2 % step), while keeping the same spatial coordinates. These random comparators are then voxelised in the same way as the initial volume. The corresponding Cr concentration histograms are then fitted with skew normal distributions, which were found to fit the statistical distributions very well. This process allows the identification of statistical parameters inherent to experimental conditions, reconstruction protocols and voxelisation methods [21] as a function of Cr concentration. The distribution of Cr concentration inside the volume can thus be written as:

$$f(C_{Cr}) = \frac{2}{\omega\sqrt{2\pi}}\, exp\left(-\frac{(x-\xi)^2}{2\omega^2}\right) \int_{-\infty}^{\alpha\left(\frac{x-\xi}{\omega}\right)} \frac{1}{\sqrt{2\pi}}\, exp\left(-\frac{t^2}{2}\right) dt \tag{1}$$

where $\xi$, $\omega$ and $\alpha$ are the location, scale and shape parameters of the skew normal distribution, respectively. Their dependence on the Cr concentration $C_{Cr}$ is determined with a polynomial regression.

Once the statistical parameters have been identified, a model must be implemented to interpret the distribution of Cr atoms inside the volume. We assume that the total distribution can be broken down into two contributions: a contribution from high-diffusivity paths, mainly GBs $H_{gb}$ and another from the unaltered multilayers $H_{ml}$. The sum of these two contributions weighted by the volume fraction of voxels altered by GBs $f_{gb}$ thus makes up the total histogram $H_{total}$ (eq. 2).

$$H_{total} = (1 - f_{gb})H_{ml} + f_{gb}H_{gb} \tag{2}$$

The first contribution $H_{ml}$ is assumed to be representative of a sine modulation of the Cr concentration, which is a reasonable assumption given the shape of the profiles in the as-received state [18]. $H_{ml}$ is thus a convolution of the statistical function $f$ in eq. (1) with a sine distribution function $g$ expressed in eq. (3).

$$g(C_{Cr}) = \frac{1}{\pi\sqrt{1 - \left(\frac{C_{Cr} - C_{Cr,0}}{A_{Cr}}\right)^2}} \tag{3}$$

where $C_{Cr}$ is the Cr concentration, $C_{Cr,0}$ and $A_{Cr}$ are the fit parameters, which are the mean Cr concentration and the Cr concentration amplitude, respectively.

The second contribution $H_{gb}$ is supposed to be representative of "GB-like" features which include GBs and other possible high-diffusivity paths. This contribution is composed of voxels of the volumes that are nearly homogeneous, *i. e.*, with concentrations close to the average concentration of the volume. It is thus a skew normal distribution centered on the average Cr concentration $C_{Cr,0}$. Finally, the sum of the two contributions is then fitted to the raw histogram (eq. 2), allowing to extract the amplitude of the concentration modulation $A_{Cr}$ (eq. 3). A two-dimensional simulation of multilayers with GBs was carried out to test the procedure (Appendix B). The results of the simulation yield an error on amplitude determination inferior to 5% when $f_{gb} \leq 0.5$.

### *2.4. Determination of interdiffusion coefficients from measurements*

To interpret the Cr concentration evolution in multilayers, the traditional Fick's second law cannot be applied because of the steep concentration gradient (small modulation wavelength $\Lambda$ of a few nanometers). In the case of a homogeneous solid solution and assuming a constant interdiffusion coefficient with concentration, the Cahn-Hilliard treatement [5] yields that the amplitude of a sine concentration modulation decays exponentially over time (eq. 4).

$$ln\left(\frac{A_{Cr}}{A_0}\right) = -D_\Lambda \left(\frac{2\pi}{\Lambda}\right)^2 t \tag{4}$$

where $A_{Cr}$ is the Cr concentration amplitude at time $t$, $A_0$ is the initial amplitude, $\Lambda$ is the modulation wavelength and $D_\Lambda$ is the interdiffusion coefficient which is a function of $\Lambda$.

For STEM-EDX and APT measurements, the interdiffusion coefficient can be directly deduced from a plot of $ln(A_{Cr})$ as a function of annealing time $t$. In the case of XRR, the relationship between intensity and interdiffusion coefficient is the following:

$$ln\left(\frac{I}{I_0}\right) = -2D_\Lambda q^2 t \tag{5}$$

where $I$ is the integral of the (000) Bragg peak at time $t$, $I_0$ is the initial intensity and $q$ is the scattering vector amplitude.

## 3. Results

### *3.1. Microstructural features*

The characterization of the samples with APT and TEM is shown in Fig. 1 as a function of annealing time. The wavelength of amplitude modulation extracted from sine fitting is found to be $\Lambda_{EDX} = 4.64 \pm 0.01$ nm in STEM-EDX and $\Lambda_{APT} = 4.69 \pm 0.05$ nm in APT, which are slightly higher than the value found with XRR measurements ($\Lambda_{XRR} = 4.50$ nm [18]). The initial profile is close to a sine curve with a Cr concentration amplitude of 11 at.%. After annealing at 440°C during 7h, the amplitude measured with

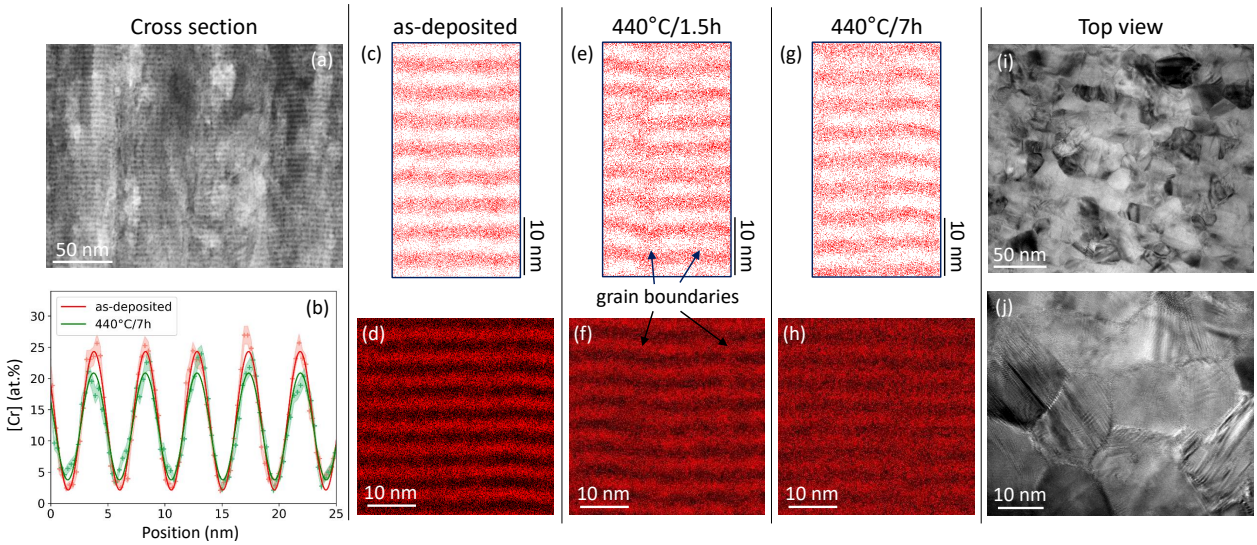


Figure 1: APT volumes and STEM-EDX maps of the as-deposited and annealed samples. (a) Cross-section view of the multilayer microstructure (STEM-HAADF). (b) Cr concentration profile across multilayers obtained with APT and corresponding sine fits. APT sub-volumes ($10\times22\times40$ nm$^3$) for the as-deposited multilayers (c) and after annealing at 440°C during 1.5h (e) and 7h (g), only Cr atoms are represented. STEM-EDX (Cr) maps for the as-deposited multilayers (d) and after annealing at 440°C during 1.5h (f) and 7h (h). (i) and (j) Top view of the multilayers revealing the grain boundaries (TEM).

APT decreased by 25%. This difference is hardly noticeable in APT volumes but is clearly distinguishable in EDX maps (Fig. 1).

Fig. 1a and Fig. 1i-j feature cross-section view and top views of the as-deposited multilayers, respectively. A high density of columnar GBs can be observed with layers sometimes bending slightly in their vicinity. A spatial distribution analysis of atoms using APT data showed that the deposition direction is close to the [111] direction. In the as-deposited state, a few Cr atoms are already segregated along GBs in Ni layers. After annealing during 1.5h, fast diffusion occurs in GBs with Cr atoms already present in Ni layers in a width of 2 to 4 nm along their normal. GBs with normals parallel to the plane of the layers constitute the main concern since they contribute to the diffusion between layers. The average grain size in this direction ranges from 10 to 20 nm, with no significant grain size enhancement during the annealing process (Table1).

| | as-deposited | 440°C/1.5h | 440°C/3h | 440°C/4.5h | 440°C/7h |
|---|---|---|---|---|---|
| TEM | 19.5 ± 1.1 | - | - | - | 19.4 ± 0.9 |
| APT | 11.9 ± 2.5 | 10.8 ± 2.3 | 15.2 ± 4.6 | 13.1 ± 2.6 | 14.0 ± 3.2 |

Table 1: Grain size (nm) along the plane of the layers measured with TEM and APT.

A minor yet significant difference in grain sizes are observed between measurements carried out with TEM and APT. This can be explained by the fact that grains are identified by the presence of segregation using APT. Large grains, which contribute to the high grain size found using TEM, were found to be divided into smaller grains with a weak misorientation between them. These low-angle grain boundaries are more

easily identifiable with APT thus contributing to a smaller grain size measurement.

### *3.2. Chemical composition*

The chemical composition measured with APT is given in Table 2. The oxygen concentration is quite high in the multilayers (approximately 1.3 at.%) and as evidenced by Table 2 already present in the as-deposited state. However, most of the oxygen is ionized in the form of CrO and NiO complex ions in the vicinity of GBs, which might indicate an initial presence of stable oxides that do not contribute to chemical diffusion inside the grains. The O concentration inside grains is estimated to be inferior to 0.2 at.%. Other impurities are present, including small amounts of Fe, C, Si, Ti and Mn. The impurity concentration does not evolve significantly as a function of annealing time, at the exception of O and C which are mostly conveyed through GBs. The purity of the multilayers is estimated to be 98 at.% overall and 99.2 at.% inside the grains. It will be noted that no significant amount of Ga was found in the reconstructed volumes, indicating that FIB preparation did not impact the analysis.

| | as-deposited | 440°C/1.5h | 440°C/3h | 440°C/4.5h | 440°C/7h |
|---|---|---|---|---|---|
| Ni | 85.1 ± 0.6 | 84.8 ± 1.1 | 86.1 ± 0.5 | 86.1 ± 0.5 | 86.0 ± 0.4 |
| Cr | 13.0 ± 0.6 | 13.1 ± 1.1 | 11.8 ± 0.4 | 11.8 ± 0.4 | 11.8 ± 0.2 |
| O | 1.22 ± 0.08 | 1.28 ± 0.07 | 1.29 ± 0.08 | 1.23 ± 0.13 | 1.26 ± 0.15 |
| Fe | 0.40 ± 0.01 | 0.43 ± 0.01 | 0.39 ± 0.01 | 0.39 ± 0.03 | 0.39 ± 0.01 |
| Si | 0.13 ± 0.01 | 0.15 ± 0.01 | 0.12 ± 0.01 | 0.11 ± 0.01 | 0.27 ± 0.23 |
| C | 0.06 ± 0.01 | 0.10 ± 0.07 | 0.14 ± 0.01 | 0.13 ± 0.03 | 0.08 ± 0.01 |
| Mn | 0.08 ± 0.01 | 0.08 ± 0.01 | 0.08 ± 0.01 | 0.13 ± 0.02 | 0.06 ± 0.01 |
| Ti | 0.05 ± 0.01 | 0.08 ± 0.02 | 0.15 ± 0.03 | 0.16 ± 0.02 | 0.08 ± 0.01 |
| Purity | 98.05 ± 0.08 | 97.89 ± 0.08 | 97.83 ± 0.09 | 97.85 ± 0.18 | 97.86 ± 0.32 |

Table 2: Chemical composition measured with APT (at.%).

### *3.3. Diffusion along GBs*

In line with the results presented above and considering the small size of the columnar grains in the multilayered material, it is clear that their existence can have a strong impact on the results and more particularly on the determination of the interdiffusion coefficient. In fact, it seems that a significant amount of diffusion occurred inside GBs as well as perpendicularly to their planes (Fig. 1). The quantification of this phenomenon inside the multilayers is difficult, given the small sizes of both layers and GBs. The large Ni layer (approximately 80 nm) is very convenient to visualize the preferential diffusion of Cr atoms inside GBs. Moreover, the GBs inside the large Ni layer own similar size and structure since they extend from the multilayers. Profiles perpendicular to GBs away from triple junctions were measured using APT inside this layer (Fig. 2).

The profiles were fitted with a normal distribution function, from which two quantities are extracted to quantitatively describe the GBs: the peak Cr concentration, which is the maximum Cr concentration

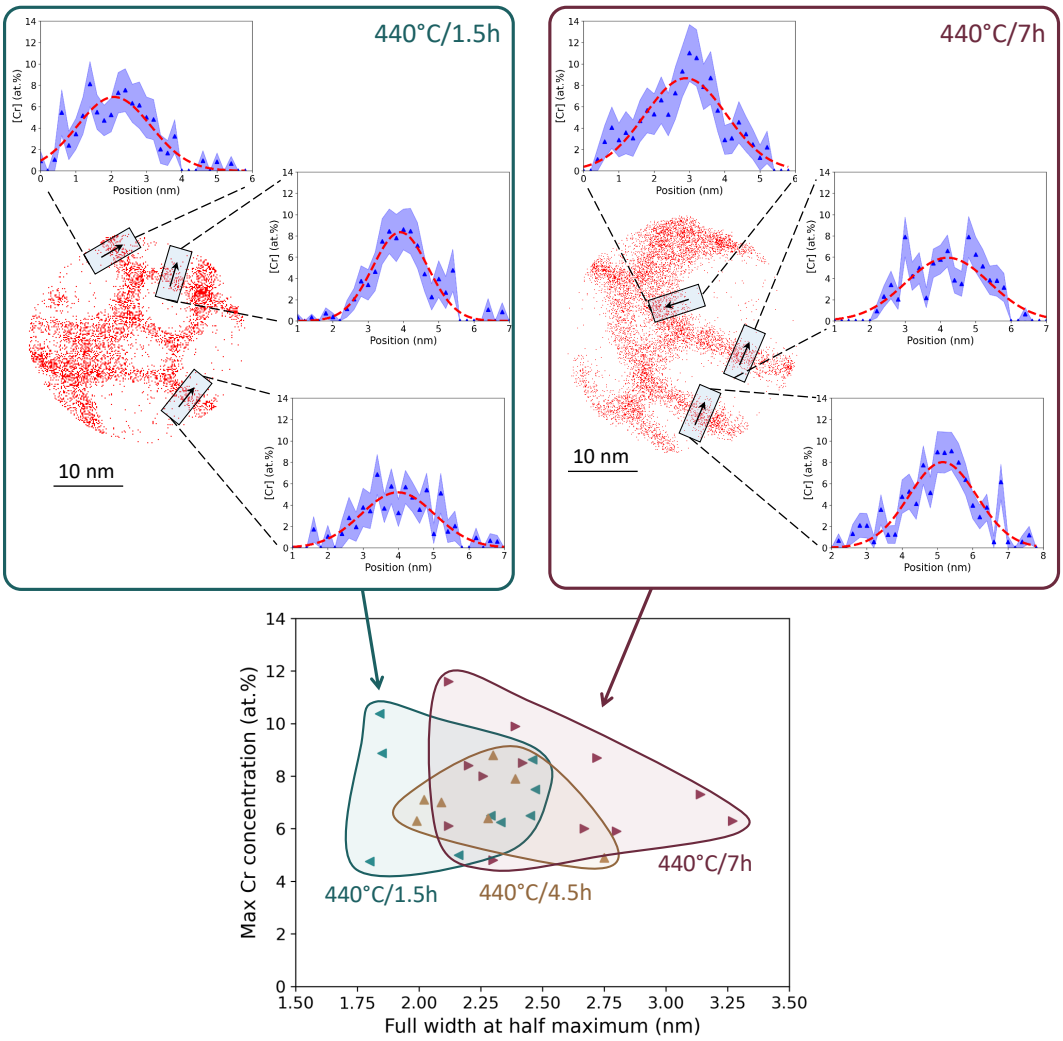


Figure 2: GB analysis using Cr diffusion inside the large Ni layer. Several Cr concentration profiles were measured through GBs using APT. A few examples of profiles for annealing times of 1.5h (top left) and 7h (top right) are given in the insets with their corresponding position inside APT volumes (only Cr atoms are shown in red). A scatter plot represents the maximum Cr concentration as a function of the Full Width at Half Maximum (FWHM) extracted from fitted profiles.

inside the grain and the Full Width at Half Maximum (FWHM). These two quantities are plotted in Fig. 2 for annealing times of 1.5h, 4.5h and 7h. It is worth noting that no Cr diffusion was observed and thus already present inside the Ni layer for the as-deposited state. After only 1.5h at 440°C, Cr atoms have already diffused along the entire Ni layer through GBs with no clear differences in concentration between the extremities and the middle of the layer. Our analysis shows that the boundaries have extended chemical widths, ranging from 1.8 nm to 3.3 nm. As a global trend, the width becomes larger with annealing time but the Cr concentration does not evolve significantly (Fig. 2). As previously stated, the measurement of the corresponding width inside the multilayers is challenging, but similar lengths can be observed in Ni and Ni20Cr layers (Fig. 1e). As a result, the volume of multilayers in interaction with GBs must be substantial.

To dissociate the contribution of GBs from the one inside the grain, a new analysis method of APT volumes was developed, referred to as the global method. It consists in the analysis of the distribution of Cr concentration inside each volume, which is extracted after voxelisation and fitted to a model (see section 2.3.4) to retrieve both contributions. A sample of raw distributions with varying annealing times is shown in Fig. 3a.

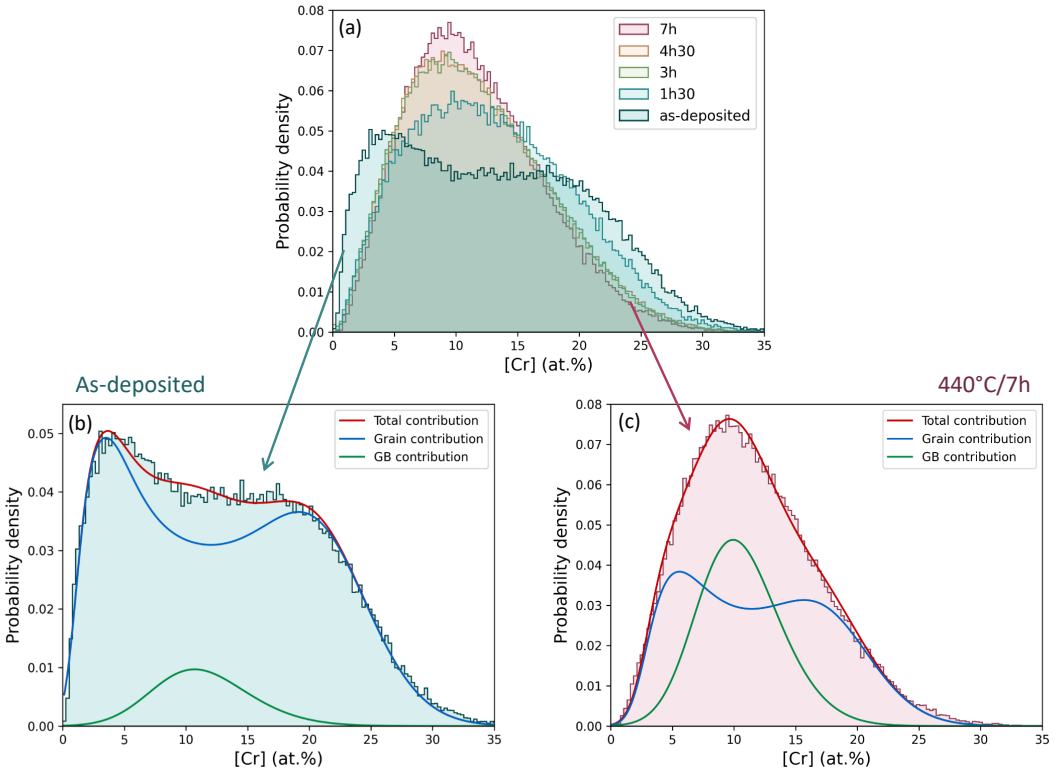


Figure 3: Global method used to determine the Cr modulation amplitude with APT. (a) Raw Cr concentration distributions, with one volume for each condition. (b) Fit of the as-deposited distribution featured in (a) with two contributions: inside the grains (referred to as Grain contribution), which corresponds to the desired sine concentration modulation, and other contributions (referred to as GB contribution) which includes GBs. (c) Fit of the distribution from the sample annealed during 7h featured in (a).

The shape of the Cr concentration histogram changes over time, with a decrease of the width of the Cr concentration distribution observed upon increasing annealing time (Fig. 3a). Moreover, a drastic change is observed between the as-deposited and the shorter annealing time (1.5h). Two peaks are clearly resolved for the former that merges into one for the latter. The fit of the histogram for the as-deposited state is shown in Fig. 3b. The grain contribution, which is representative of the diffusion between layers in areas not disturbed by GBs, is clearly dominant in the as-deposited state. The other contribution, which is mainly representative of diffusion inside and perpendicularly to GBs, becomes significant only after thermal annealing.

*3.4. Cr concentration amplitude and interdiffusion coefficient*

| | $I/I_0$ XRR | $A_{Cr}$ EDX | $A_{Cr}$ APT local | $A_{Cr}$ APT global |
|---|---|---|---|---|
| as-deposited ($t_0$) | 1.000 | 4.2 ± 0.3 | 11.2 ± 0.5 | 10.9 ± 0.2 |
| 440°C/1.5h | 0.238 | 3.2 ± 0.4 | 9.7 ± 0.5 | 9.7 ± 0.6 |
| 440°C/3h | 0.181 | 2.2 ± 0.2 | 9.4 ± 0.4 | 9.7 ± 0.2 |
| 440°C/4.5h | 0.155 | 1.5 ± 0.2 | 8.6 ± 0.7 | 9.4 ± 0.5 |
| 440°C/7h | 0.142 | 1.2 ± 0.1 | 8.3 ± 0.6 | 9.2 ± 0.5 |
| $D$ (with $t_0$) | - | 25.6 ± 2.8 | 6.2 ± 1.4 | 4.3 ± 0.9 |
| $D$ (without $t_0$) | 7.1 ± 1.6 | 22.5 ± 4.4 | 4.2 ± 0.9 | 1.6 ± 0.5 |

Table 3: Normalized intensities $I/I_0$ measured with XRR, Cr modulation amplitudes $A_{Cr}$ (at.%) measured with STEM-EDX and APT (local and global methods). The corresponding interdiffusion coefficients $D$ ($10^{-24}$ $m^2/s$) determined with each technique is given in the corresponding column.

The relative peak integrals measured with XRR as well as the amplitudes measured with the other techniques are given in Table 3. A significant decrease in intensity is observed in XRR after the first annealing, which does not seem to exist with the other techniques. The amplitude measured with both APT methods are consistent with each other considering uncertainties. However, STEM-EDX amplitudes are significantly lower than the ones measured by APT. The variability of measurements is larger in APT (Fig. 4c), which demands a high experimental effort to lower the uncertainties. At least 5 different volumes consisting of 5 million ions or more are required to obtain statistically valid results. Since the amplitude are very close from each other, especially in the case of the APT global method, a new annealing was performed at 440°C during 65h in order to validate the interdiffusion coefficient measurement. The measured amplitude is in excellent agreement with the previous points ($A_{Cr} = 5.6 \pm 0.1$).

The major drop in intensity observed in XRR after the first annealing, which is probably characteristic of a first fast regime of diffusion, prohibits the use of the as-deposited state ($t_0$) for the calculation of the interdiffusion coefficient. It was thus calculated with and without taking into account the initial state (Table 3 and Fig. 4). Taking into account the initial state always leads to higher interdiffusion coefficients, which tends to point out that it shouldn't be included in its calculation. The main finding is that $D$ strongly depends on the technique used, with the following order: $D_{EDX} > D_{XRR} > D_{APT,local} > D_{APT,global}$.

## 4. Discussion

*4.1. Comprehensive description of diffusion inside the multilayers*

*4.1.1. Lattice diffusion*

Lattice diffusion is the phenomenon of interest in this study. However, it also is the slowest diffusion mechanism at work in the multilayers, especially at the temperature of study [17]. Thus the contribution of lattice diffusion must be the one that is left when the contribution of other mechanisms (mainly diffusion along high-diffusivity paths) are dismissed. Moreover, the contribution of each mechanism should be different

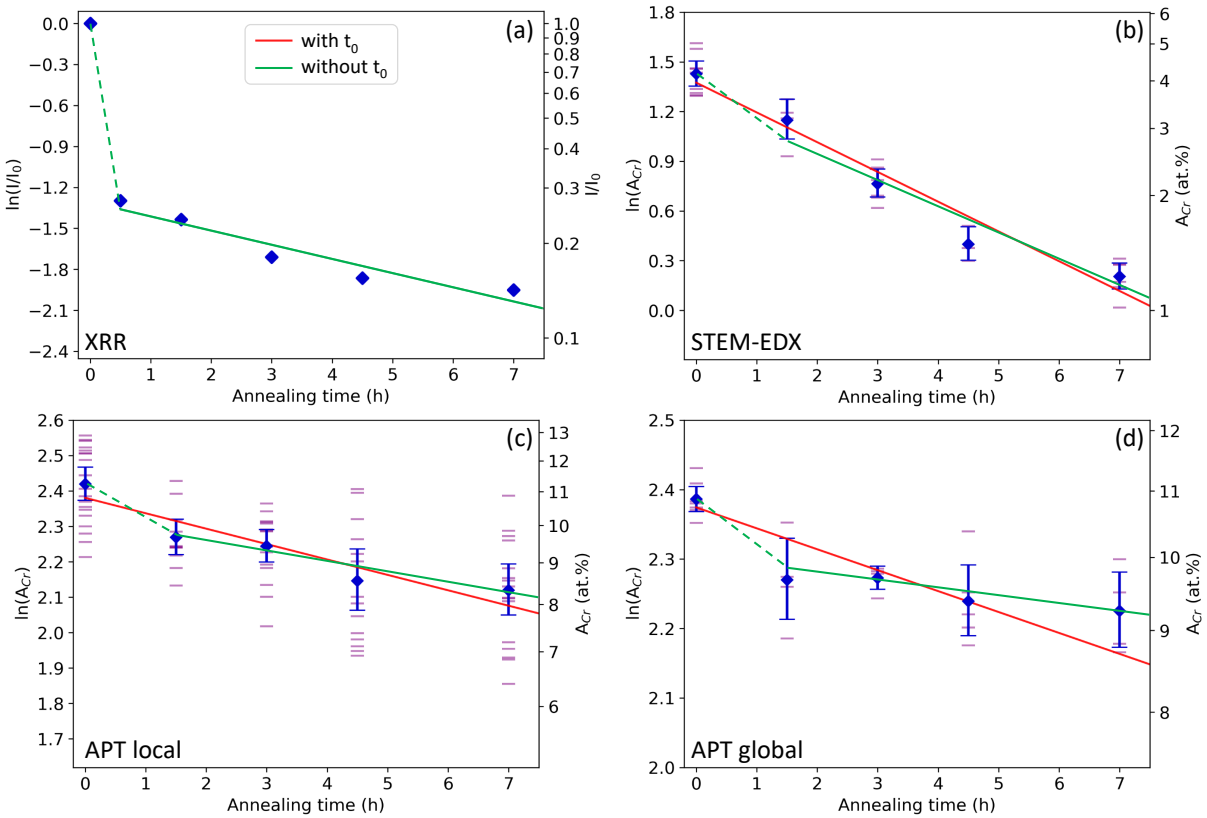


Figure 4: Interdiffusion coefficient determined with the different techniques: (a) XRR, (b) STEM-EDX, (c) APT local method and (d) APT global method. The green and red lines represent fitting of data with and without taking into account the as-deposited state ($t_0$), respectively. Small purple lines represent individual data points and blue diamonds mean of measurements.

for each characterization technique since they probe different amount of volumes. We already established the presence of two regimes, the second regime being attributed to lattice diffusion inside the multilayers. In systems with a strong asymmetry between tracer diffusions, the net volume flux of atoms in a given direction during interdiffusion can cause a build up of diffusion-induced stresses eventually leading to a decrease in the measured diffusion coefficient [22]. This phenonemon can produce two distinct diffusion regimes, with a second transient dominated by the slower species kinetics [23]. However, the difference in mobility and partial molar volumes of both species is too small in the Ni–Cr system [24, 25] to witness such an effect. The second regime can thus be reasonably attributed to lattice interdiffusion, as previously stated.

*4.1.2. Short-circuit diffusion*

The main source of short-circuit diffusion paths is the large concentration of GBs. As a global trend, the diffusion inside GBs in fcc metals is several orders of magnitude larger than inside the lattice [26]. However, GB diffusion can vary greatly depending on the nature and orientation of the GB [27–31]. In the present study, the orientation of the grains in the multilayers are such that the [111] direction is close to the deposition direction. This fiber-texture is typical of deposited thin films in fcc metals [16].

An extensive literature exists on grain-boundary diffusion in Ni and Ni–Cr binary alloys [31–33]. Gheno *et al.* measured the diffusion of Cr in Ni inside high-angle GBs in the 346-668°C temperature range [31]. Extrapolation of their measurements yields a rough estimate of Cr diffusion inside GBs of $5 \times 10^{-18}$ m$^2$/s at 440°C, which is 6 orders of magnitude higher that the measured interdiffusion coefficients (Table 3). This explains the rate at which GB diffusion occurs, with an equilbrium Cr concentration already reached at the center of the large Ni layer after only 1.5h (Fig 2). However, this particular experiment was performed on high-purity materials, which is far from our case given that the impurity level is quite high (Table 2) and mostly segregated at GBs. In fact, impurities can greatly alter diffusivity at GBs, especially at low temperatures [34, 35]. In all cases, given the high GB diffusion rate inside the large Ni layer and the small distance between layers inside the multilayers (half a wavelength or roughly 2.3 nm), it is reasonable to assume that the GBs are homogenized in a few seconds at this temperature. It is even extremely likely that the GBs homogenization process already started during deposition, at least at triple junctions, which usually exhibit higher diffusion coefficients [36].

From the observation of diffusion in the large Ni layer, it is obvious that the chemical width of GBs is much larger than the one measured with diffusion experiments in fcc metals, which is typically found to be close to 0.5 nm [17, 26, 35, 37]. After annealing at 440°C during 1.5h, the chemical width is roughly equal to 2.2 nm and appears to gradually increase with annealing time (Fig. 2). Reconstruction artefacts are an important factor to take into account in order to validate a width measurement with APT. The presence of interfaces with a varying chemical concentration can lead to local magnification effects [21], causing a biased determination of the interface width and composition. This effect can be visualized by local variations of the atomic density in 1D profiles. The examples of two distinct profiles through GBs are given in Fig. 5.

The profiles through GBs show an increase of the atomic density in the Cr-rich boundary, which indicates that GBs constitute a low-field region. The presence of a low-field region leads to an underestimation of the apparent width of a 1D profile by creating a low-curvature area on the surface of the tip [38]. However, this effect can be corrected by taking into account the local density. Sauvage *et al.* proposed that the distance should be scaled linearly with atomic density to obtain a corrected profile [39]. This method was used to calculate corrected profiles (Fig. 5). The difference between the initial and corrected profiles is usually small but can result in significant corrections, as shown in Fig. 5b. In any case, the apparent chemical width of GBs measured in the large Ni layer (Fig. 2) is slightly underestimated and constitutes a lower bound. The presence of an extended chemical width of the GB is thus a real feature of the sample. Such extended chemical widths of GBs were already observed using APT in Ni–Cu [36] and PtIr–Cr [40] thin films. It is also a common feature of GBs found in additively-manufactured alloys, which produce strongly out-of-equilibrium microstructures [41]. In our case, it is not clear whether the extended profiles are the result of equilibrium or non-equilibrium phenomena. Some of the profiles seem to exhibit an oscillatory

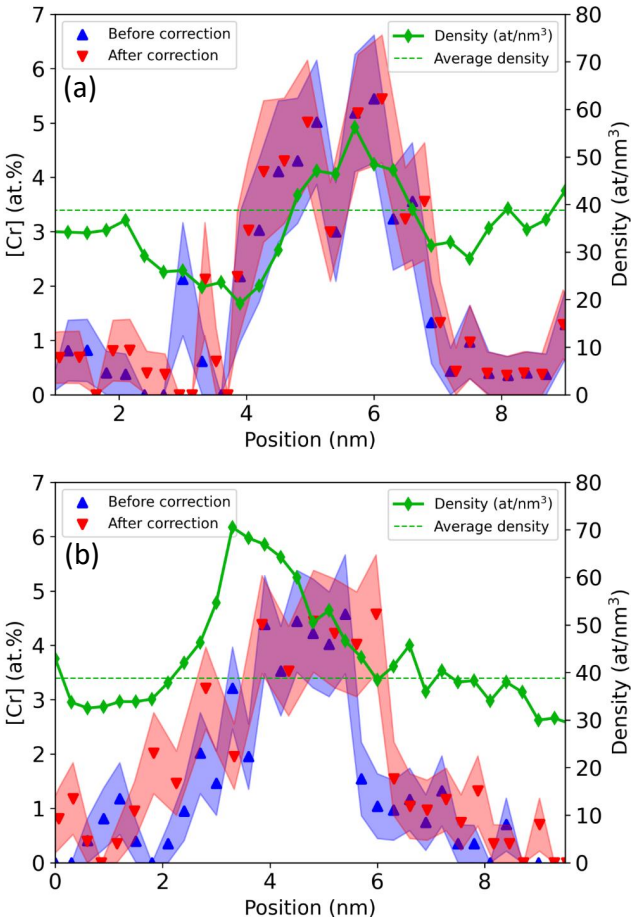


Figure 5: 1D Cr concentration profiles through GBs in the large Ni layer after annealing at 440°C during 1.5h. The atomic density is represented (green curve and diamonds) to highlight its non-uniformity through the profile. The initial profiles are shown and compared with corrected profiles, assuming a linear variation of the local magnification effect with atomic density. Two examples are shown (a) profile leading to a negligible correction, (b) profile leading to a significant correction (superior to 1 nm).

trend (Fig. 2), which can exist in alloys with an ordering tendency. Startt *et al.* evidenced an oscillatory segregation trend at low index surfaces in fcc Ni–Cr alloys using DFT calculations: enrichment in Ni at the first plane then enrichment in Cr at the second plane from the surface [42]. Such a phenomenon could explain a wide equilibrium segregation profile in high-angle grain boundaries.

Since the grain size is not so large (Table 1) compared to the segregation width of GBs, it should have a significant impact on the measurements. Once GB diffusion has taken place and the segregation width has been filled, diffusion should occur along the normal of GBs with the rate of lattice diffusion. Considering that the lattice interdiffusion coefficient is equal to $5 \times 10^{-24}$ m$^2$/s, then the characteristic diffusion enlargement of the profile expressed as $2\sqrt{2Dt}$ ranges from 0.4 nm to 1.0 nm, consistent with measurements inside the large Ni layer. In the Harrison classification [43], the multilayered material is thus at the limit between

B (significant lattice out-diffusion from GBs) and C ("frozen" lattice diffusion) regimes and the impact of lattice diffusion in the vicinity of GBs has to be considered.

*4.1.3. Lattice diffusion in the vicinity of grain boundaries*

Lattice diffusion in the vicinity of GBs is of paramount importance considering the small size of the grains. It can be described as a "leak" of atoms through the GB segregation zone which are free to diffuse perpendicularly to its plane. Its effect is to progressively homogenize the layers adjacent to GBs. Another important aspect of diffusion in proximity of GBs is grain growth, which can have a significant impact since an immobile boundary is a less effective diffusion path than a moving one [44]. In thin films, grain growth can be quite significant even at relatively low homologous temperature [45–47]. However, no clear signs of grain growth was observed in our samples (Table 1). It is hypothesized that it could be caused by precipitation of small oxides inside GBs in the first moments of annealing, which would strongly hinder grain growth by Zener pinning [48]. In fact, the O solubility is very low in Ni, in the order of 5 appm to 50 appm, as evidenced by Perusin *et al.* [49] and Poplawsky *et al.* [50]. It is not clear whether such precipitation can have a significant impact on GB diffusion. The study of Rajeshwarie *et al.* [51] emphasizes the complexity of such phenomena, as structure, morphology, segregation and precipitation are often correlated in making differences in GB diffusion coefficient. Another possibility is that the attraction between segregated atoms (such as O) and GBs is so strong that it completely impedes GB motion by the so-called solute drag phenomenon [52, 53]. In our material, there is not evidence of significant differences in oxygen concentration between different GBs. However, it appears that the Cr concentration vary from boundary to boundary (Fig. 2), which may be caused by the co-existence of several complexions with different equilibrium segregation concentrations [54–56].

Considering grain growth as negligible and once the equilibrium concentration is attained, the GB can be described as a constant source of atoms, which dampens the concentration amplitude concomitantly to diffusion between the layers themselves. Diffusion inside a mulitlayered material with a nanometric-scale grain size and with grains perpendicular to the layers is a special case of diffusion inside nanocrystals [17]. Given the small diffusion lengths and important diffusion coefficients inside GBs, GB diffusion will become imperceptible after a few seconds. For this reason, the accepted Hart equation for nanomaterials [17, 57] does not apply in this case. A schematic representation of the geometry of diffusion is presented in Fig. 6.

The volume fraction of multilayers unaltered by GBs ($V_{ML}$) over the total volume ($V_T$) decreases over time. To examine the evolution of this volume fraction and its impact on measurements, a model is developed where grains are prismatic with a grain size $g_s$. The development of the model is described in Appendix A. Given that the segregation width is different from the diffusion width, there is no way of knowing at which rate diffusion occurs from the core of the boundary to the segregation zone. We will thus only consider diffusion from the segregation area of the GB to the bulk, considering that the segregation area is already

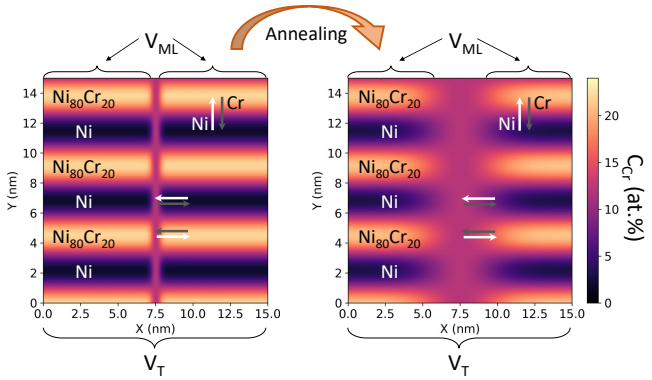


Figure 6: Schematic representation of the geometry of diffusion inside multilayers with a GB at the center. Assuming a negligible segregation of Cr atoms in GBs, diffusion occurs both perpendicularly to GBs and between the layers themselves. This process impacts the concentration modulation amplitude in the vicinity of GBs. The volume fraction of multilayers unaltered by GBs ($V_{ML}$) over the total volume ($V_T$) decreases over time.

saturated after the first annealing condition ($t = 1.5$ h). The volume fraction of GB $f_{gb} = 1 - (V_{ML}/V_T)$ increases over time and can be written as (Appendix A):

$$f_{gb} = 1 - \left(1 - \frac{\delta_s + 3\sqrt{Dt}}{2\,a\,g_s}\right)^2 \tag{6}$$

with $\delta_s$ the segregation width of the GB, $D$ the interdiffusion coefficient, $t$ the annealing time, $g_s$ the average grain size and $a = \sqrt{\frac{\pi}{8\sqrt{3}}} \simeq 0.476$ a geometric parameter.

*4.2. Difference in amplitude and interdiffusion coefficient between STEM-EDX and APT*

The difference in amplitude between STEM-EDX and APT (Table 3) can be explained, at least partially, by the waviness of the layers. It is quite clear that the layers are not perfectly straight, even in the as-deposited sample (Fig. 1). These slight fluctuations are admittedly present in the depth of the thin foil. This feature can lead to a dampening of the measured amplitude, even if the layers are perfectly aligned with the electron beam. This effect can be simulated schematically by considering that the waviness of the layers follows a sine function and that the probe size is infinitely small (limit case). The simulated measured amplitudes as a function of the true amplitude is shown in Fig.7a (solid red line) for a geometry representative of the samples, based on STEM observations.

It is interesting to notice that the model predicts a proportional relationship between the true and measured amplitudes. Even if the model is simplistic, a real waviness (much more chaotic) should produce similar result but with a variability depending on the area on which the analysis is carried out. This implies that the measured interdiffusion coefficient should not be impacted since $ln\,(A_{Cr})$ varies linearly with annealing time. However, the interdiffusion coefficient measured with STEM-EDX is significantly superior to the one measured with APT, which means that there should be something else that influences the measurements.

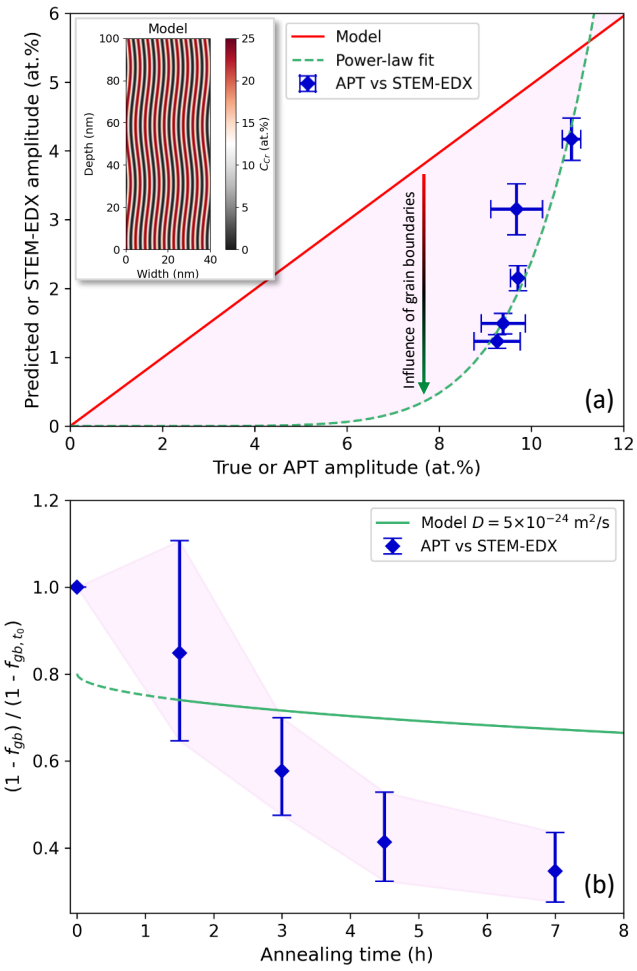


Figure 7: Modeling of the amplitude measured by STEM-EDX. (a) Predicted amplitude versus true amplitude (straight red line). The model considers that the waviness of the layers follows a sine function (amplitude of 1.08 nm and period of 55 nm) in the depth of the thin foil. A schematic representation of the geometry of the layers is shown in the inset. The experimental STEM-EDX and APT amplitudes are also shown (blue diamonds). (b) Evolution of the volume fraction of multialyers unaltered by GBs $(1 - f_{gb})$, assuming that the relationship between STEM-EDX and APT amplitudes can be written as in eq. (7). The model described in equation (6) is represented for an average grain size $g_s = 15$ nm and $\delta_s = 1.5$ nm and $D = 5 \times 10^{-24}$ m$^2$/s (solid and dashed green line).

In fact, a completely different trend is observed when APT and STEM-EDX measurements are added to this graph (Fig. 7a), considering that the former is representative of the true amplitude. Diffusion perpendicular to GBs (Fig. 2) probably has the effect of dampening the apparent amplitude even further as a function of annealing time. The grain size ($\simeq$ 15 nm) is small compared to the thickness of the thin foil ($\simeq$ 100 nm), such as that several GBs are expected to be present within its core. Assuming a proportional relationship between APT and STEM-EDX amplitudes for the as-deposited state as presented in the model and a linear influence of GBs, the amplitude measured in EDX $A_{EDX}$ follows the form:

$$A_{EDX} = p\,(1 - f_{gb})\,A_{APT} \tag{7}$$

where $p < 1$ is the proportionality coefficient due to the curvature of the layers.

With the help of experimental data and eq. 7, the evolution of the volume fraction of multilayers unaltered by GBs ($1 - f_{gb}$) can be assessed (Fig. 7b). A steep decrease of this quantity with annealing time is observed, superior to the one expected from the model developed in section 4.1.3. Considering the grain size and the apparent interdiffusion coefficient in the multiayers, a decline of this magnitude is very unlikely. This could be explained by a waviness that varies over time. Layers are observed to bend slightly in the vicinity of grain boundaries during annealing, probably to accommodate stresses. The high interdiffusion coefficient measured with STEM-EDX is thus a result of diffusion inside and in the vicinity of GBs combined by a time-dependent waviness of the layers.

The analysis of STEM-EDX results is made notably complex as a result of the thickness of thin foils needed to obtain a signal worthy of quantification. In fact, the two relevant parameters to a STEM-EDX analysis of multilayers are the grain size and the concentration modulation wavelength. The larger these parameters are, the more suitable becomes the EDX analysis. A parameter assessment of the model presented in Fig. 7a shows that, for the same waviness, a difference between measured and true amplitudes of 13% is obtained for a wavelength of 10 nm. This figure even drops down to 5% for a wavelength of 15 nm. Ideally, the thickness of the thin foil should be similar to the grain size.

*4.3. Difference in interdiffusion coefficient between XRR and APT*

Since XRR does not provide a direct measure of the concentration modulation amplitude, the comparison between APT and XRR must be carried out on the interdiffusion coefficient without taking into account the as-deposited state ($t_0$). The difference between both values is small, yet meaningful since the consideration of uncertainties clearly differentiates them (Table 3).

The main distinction between the two techniques originates from the significant difference in analysis volume. While XRR probes and averages over more than $5 \times 10^{15}$ nm$^3$, one APT profile with the local method represents a volume of only $2.7 \times 10^3$ nm$^3$. APT measurements are thus sensitive to local grain sizes, crystallographic orientations, localized waviness and in general to local features of the microstructure. This is the major drawback of APT analysis, which therefore requires a high experimental investment, needed to average all of theses contributions.

However, an analysis at a small scale can provide useful informations, mainly on high-diffusivity paths that are of primary concerns in diffusion experiments at low temperature. The model developed in section 4.1.3 can provide a few hints towards an understanding of the interdiffusion coefficient measured with XRR. From the examination of the results, it can be stated that as the Cr concentration amplitude decreases, the total volume of multilayers decreases concomitantly, as expressed in eq. 6. Assuming that the intensity measured with XRR is proportional to the volume fraction of multilayers, equation (5) can be corrected by

taking into account this last contribution (eq. 8).

$$ln\left(\frac{I}{I_0}\right) = -2D_\Lambda q^2 t + ln\left(\frac{V_{ML}}{V_T}\right) \tag{8}$$

The APT global method is of particular interest since it allows the determination of a fraction of GB in the volume through the fit of the histogram (eq. 2). The volume ratio of multilayers over the total ratio ($V_{ML}/V_T = 1 - f_{gb}$) extracted from APT histograms, as well as direct measurements of $f_{gb}$ from the large Ni layer are represented in Fig. 8. Since the values of $f_{gb}$ measured with the global method is supposedly representative of other features than GBs (such as APT poles), which do not depend on time, the corresponding values of $f_{gb}$ are normalized by their initial values.

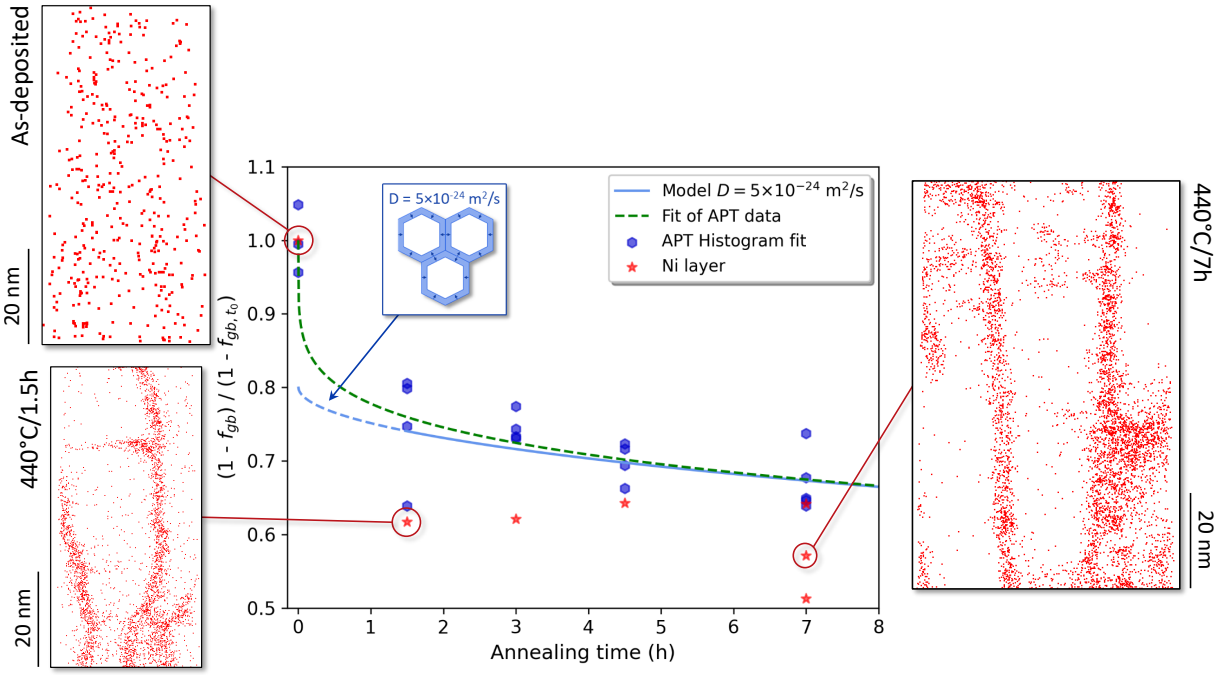


Figure 8: Evolution of the volume ratio of multilayers over the total ratio ($V_{ML}/V_T = 1 - f_{gb}$) extracted from APT histograms (blue hexagons) and from Ni layers (red stars) normalized by the initial ratio. The APT histogram data are fitted with a power-law (dashed green line). The model described in equation (6) is represented for an average grain size $g_s = 15$ nm, $\delta_s = 1.5$ nm and $D = 5 \times 10^{-24}$ m$^2$/s (solid and dashed blue line). APT volumes corresponding to some datapoints in the large Ni layer are shown in the insets on the sides (only Cr atoms are represented in red). The size of Cr atoms in the as-deposited volume has been increased for visualization purposes.

The normalized GB volume fractions are higher in the Ni layer in comparison to the multilayers (Fig. 8). It is likely that the grain-boundary thermal segregation is higher in the large Ni layer since a dependence of its magnitude on Cr is expected. This phenomenon could facilitate the outward diffusion of Cr in pure Ni grains, thus resulting in a larger value of $f_{gb}$. However, the segregation behavior should be highly disturbed due the high O concentration inside GBs. The small diffusion lengths in the multilayers, unlike in the Ni layers could also provide a pragmatic explanation. The GBs in the multilayers are expected to be already

slightly homogenized in the as-deposited state, which translates into a non-zero value of the grain-boundary contribution of $f_{gb}$ in the initial state. This is noticeable to some extent in the APT volumes (Fig. 1) and on the histograms of the as-deposited state (Fig. 3). Nevertheless, those two sets of values are in good agreement with each other, confirming the validity of the APT global method.

The model described in equation (6) is plotted in Fig. 8 with $g_s = 15$ nm (Table 1), $\delta_s = 1.5$ nm (Fig. 2) and $D = 5 \times 10^{-24}$ m$^2$/s (Table 3). These parameters fit experimental data in a reasonable manner for annealing times superior to 1h. The description of the GB with an extended segregation width that fills out swiftly followed by a second regime during which diffusion occurs perpendicularly to this interface reproduce experimental data well. However, it does not provide a complete picture since the mechanisms at play and their corresponding rates at which this segregation occurs are unknown.

After 1.5h at 440°C, a drop in intensity of roughly 75% is measured with XRR. The analysis developed above allows us to evaluate the impact of GB diffusion on this intense drop. Clearly, GB diffusion cannot explain the entirety of the phenomenon. From the investigation presented in Fig. 8, the GBs can explain a maximum of 35% of intensity decrease. The combination of the drop in amplitude reported with the APT global method (Fig. 4) and the influence of GB diffusion can account for a maximum of half of the first drop in intensity. Some other mechanism specific to XRR measurements must be at play, which will be discussed later.

During the steady state regime, diffusion perpendicularly to GBs has a limited yet significant impact in our case (Fig. 8). The contribution of lateral diffusion from GBs and the equivalent contribution of lattice diffusion in grain-boundary-free multilayers can be separated with the use of equation (8) combined with direct measurements (Fig. 8) and/or the use of a simplistic model, as developed in Annex B. From the use of data collected here, the interdiffusion coefficient detemined with XRR ($7.1 \times 10^{-24}$ m$^2$/s) can be corrected to $5.2 \times 10^{-24}$ m$^2$/s (eq. 8). The difference is small, as $f_{gb}$ does not evolve much during annealing. However, this lower value is in better agreement with APT measurements (Table 3).

### *4.4. Final assessment of lattice interdiffusion coefficient in Ni11Cr*

The results point towards the existence of a fast first regime of diffusion, independent from short-circuit diffusion effects, which prohibits the use of the as-deposited state in the calculation of the interdiffusion coefficient. Since probe-corrected STEM-EDX is susceptible to complex microstructure effects, this technique is not appropriate for the diffusion measurements inside multilayers with a combination of a small concentration modulation wavelength and small grain size. XRR ($7.1 \times 10^{-24}$ m$^2$/s) and APT global method ($1.6 \times 10^{-24}$ m$^2$/s) yield different result even considering experimental uncertainties. As demonstrated in this paper, the APT global method is less sensitive to grain boundary effects. Moreover, the examination of an extensive annealing time (440 °C/65h) supports the interdiffusion coefficient measured with the APT

global method. The value provided by this method is thus assessed to be the most accurate measure of interdiffusion in Ni11Cr (at.%): $1.6 \pm 0.5 \times 10^{-24}$ m$^2$/s.

*4.5. On the measurement of interdiffusion in multilayered systems*

As we previously established, the first drop in intensity observed with XRR cannot be entirely accounted for with GB diffusion and amplitude mitigation inside the multilayers. Such an impressive drop in intensity in the first moments of annealing have already been reported in other multilayers [10, 58–60]. Multiples causes were invoked by the authors to justify this phenomenon: GB diffusion, grain growth and recrystallization. However, in our case with no grain growth nor recrystallization and GB diffusion accounted for, a drop in amplitude still exists with APT. This rapid decrease in amplitude may be explained by an acceleration of diffusion caused by an initial excess of point defects after the deposition process. Another possible explanation is the oxidation at GBs, which can create a flux of vacancies into the volume of the grains [1]. In any case, taking into account both GB effects and first amplitude regime, only half of the first drop in intensity was able to be explained. Since stress-mediated diffusion was already ruled out, some other mechanism specific to XRR measurements must be at play, such as an evolution of the surface roughness, strain relaxation, oxidation of the surface or the presence of sharp initial interfaces between layers. The latter hypothesis seems plausible since APT is prone to reconstruction artefacts due to a difference in evaporation fields between the layers [61, 62], which can result in a smoothing of interfaces. This effect should be limited since no significant differences between the atomic densities of Ni and Ni20Cr was observed.

The comprehensive characterization described in this study allows us to state that multilayers are a good way to measure interdiffusion coefficients at low temperatures. However, there are some limitations inherent to the process. Firstly, the temperature window is very restricted for a given modulation wavelength. On the one hand, annealing at high temperatures will cause a homogenization of the multilayers in a few seconds. On the other hand, diffusion at a low enough temperature will become too sluggish to measure it in a reasonable time frame. Unwanted mechanisms can become preponderant after extended annealing times such as oxidation, because of the small scale of the thin film. A good set of conditions to follow are (C1): $A(t = 200h)/A_0 < 0.9$ and (C2): $A(t = 1h)/A_0 > 0.75$. For the present system, these values were calculated using extrapolations of higher temperature data [18]. These two limit cases can be plotted in a wavelength versus temperature diagram (Fig. 9). It can be noticed that the temperature window is very limited for a given wavelength in the Ni–Cr system: roughly 100°C.

Another critical component is the complex microstructure created by the deposition process, which introduces a second limitation. The strength of the multilayers is that its concentration homogenization rate will tend towards the lattice diffusion coefficient after a given amount of time as other contributions (diffusion along GBs and dislocations) will run out. However, to ensure that they will, a few conditions must be met. The results of the present study highlight a possible strong influence of the microstructure

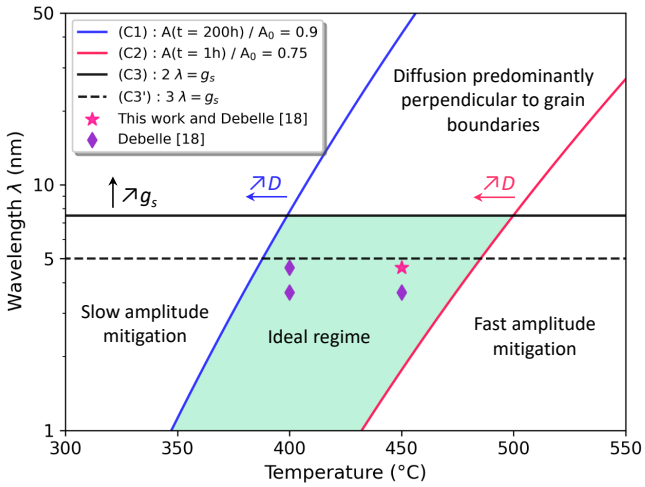


Figure 9: Wavelength versus temperature diagram, allowing to visualize the ideal regime for the determination of lattice interdiffusion coefficient inside multialyers. The interdiffusion coefficients were calculated using extrapolations of higher temperature data [18]. The grain size is taken as $g_s$ =15 nm.

on the measurement of the interdiffusion coefficient. In some cases, diffusion perpendicularly to GBs can be significant and change the geometry of diffusion inside the multilayers (Fig. 6), thus introducing a bias in measurements. Given that diffusion between layers as well as diffusion between GBs and bulk depend on the lattice interdiffusion coefficient, the contribution of diffusion perpendicularly to GBs does not depend on temperature but rather on the ratio of the modulation wavelength $\Lambda$ over the grain size $g_s$. Assuming that the segregation width is small compared to the grain size, the multilayers will homogenize in the direction perpendicular to the layers at high values of this ratio ($\Lambda \ll g_s$). Conversely ($\Lambda \gg g_s$), they will homogenize in the direction parallel to the layers after a GB diffusion regime. It can also be noted that another regime at large wavelength ($\Lambda > 50$ nm) and small grain size (as in our study) could be used to measure interdiffusion coefficient inside GBs at very low temperatures [63]. A simple analysis reveals that with a high-resolution technique such as APT, which will allow to distinguish the contribution of GBs to the one of the bulk (C3): $2\Lambda < g_s$ is a sufficient condition (Fig. 9). For other techniques such as XRR, a safer condition would be (C3'): $3\Lambda < g_s$. If this last condition is too restrictive, the simple analysis developed in this study can help to produce a rough correction of the interdiffusion coefficient with the help of equations (6) and (8). In between all these conditions, lies a region (filled in green in Fig. 9), where the conditions are ideal for the measurement of interdiffusion coefficients with multilayers. As it turns out, the multilayers of the present study fall in the ideal regime, very close to the $3\Lambda = g_s$ limit condition. This explains why the correction of XRR measurements is small and thus validates the conditions developed in this section.

It can be noted that a similar reasoning can be applied in the case of multilayers with no GBs, such as thin films produced by molecular beam epitaxy. They usually exhibit a microstructure with the presence of misfit dislocations, which act as high-diffusivity paths [14]. In this case, an expression similar to eq. (6) can

be derived with the average spacing between dislocations replacing the grain size $g_s$ as the key parameter.

## 5. Conclusions

The interdiffusion of Cr and Ni in the fcc Ni-rich side of the Ni–Cr system was investigated at 440°C using Ni-Ni20Cr multilayers produced by magnetron sputtering. Anneals were performed during 1.5h to 7h and the resulting multilayered material was characterized using atom probe tomography (APT) and energy-dispersive X-ray spectroscopy (EDX). The obtained results were compared with X-ray reflectivity (XRR) measurements [18]. For the first time, we conducted a comprehensive atomic-scale study investigating the evolution of the multilayers microstructure with annealing time, allowing a reliable appreciation of the mechanisms at play. From the results obtained in this study, the following conclusions can be drawn:

1. A high density of columnar GBs was observed, with extended chemical widths (superior to 1.5 nm) after 1.5h at 440°C.
2. The sequence of mechanisms at play in multilayers with columnar GBs has been brought to light. A first fast regime during which diffusion occurs along GBs contributes to the homogenization of a high volume fraction of the material. It is then followed by a second regime during which lattice diffusion operates between GBs and the multilayers concomitantly to between the layers themselves.
3. The measured interdiffusion coefficient $D$ is dependent from the technique used, with the following order: $D_{EDX} > D_{XRR} > D_{APT}$. It was shown that both EDX and XRR are sensitive to grain-boundary diffusion caused by averaging over a high volume of material.
4. A new method was developped for the determination of the concentration modulation amplitude in multilayers, based on the voxelisation of APT volumes. It allows the generation of a concentration distribution inside the volume that can be interpreted by a simple model. This method further allows to dissociate the contribution of diffusion in the vicinity of GBs from the contribution of lattice diffusion between layers, thus yielding the true concentration modulation amplitude. It could easily be extended to more complex systems, such as ternary multilayers
5. XRR measurements were found to provide a good estimate of the lattice interdiffusion coefficient. However, it always yields an upper bond of its value because it averages over grain-boundary diffusion and lattice diffusion in the multilayers as well as perpendicularly to GBs (lateral diffusion).
6. A simple geometric model is derived to correct XRR measurements from lateral diffusion, which yields a value in better agreement with APT measurements.
7. From the analysis of all results, the interdiffusion coefficient in Ni11Cr (at.%) at 440°C is assessed to be $1.6 \pm 0.5 \times 10^{-24}$ m$^2$/s.
8. The analysis of all parameters relevant to multilayers reveals that the temperature window to measure the lattice interdiffusion coefficient is mostly limited by the ratio of the concentration modulation

wavelength over the grain size. At high values of this ratio ($\Lambda \ll g_s$), the multilayers will homogenize in the direction perpendicular to the layers. Conversely ($\Lambda \gg g_s$), they will homogenize in the direction parallel to the layers after a GB diffusion regime.

**Acknowledgments**

This work has been partially funded by the CNRS-NEEDS program and by the European Commission HORIZON 2020 Framework Program under the grant agreement No. 755269 (GEMMA). It has been carried out in the frame of the French National Research Agency, under the "Investissements d'avenir" program (No ANR-11-EQPX-0020). The research was supported by the Cross-cutting basic research Program of Division Energy of CEA (RTA Program), the RMATE project (CEA) and the cross-cutting exploratory bottom-up program (CEA).

## Appendix A. Modeling of diffusion perpendicularly to GBs

We consider a grain of prismatic shape with hexagonal base characterized by a chemical width $\delta_s$ and a grain size in the plane of deposition $g_s$ (Fig. A.10). In the case of multilayers, with very small diffusion lengths inside GBs, the GB can be modeled as a constant source of atoms in dynamic equilibrium. In this case, the general solution of diffusion perpendicularly to this source is a complementary error function. To set a volume fraction of grains that are altered by diffusion in the vicinity of GBs, one has to make an arbitrary choice of the diffusion distance. In the case of the error function, a diffusion length equal to $\sqrt{Dt}$ corresponds to an amplitude reduction of 48%, which is not restrictive enough considering that the total Cr concentration amplitude was roughly reduced of 25% from the initial to the final state (Table 3). The diffusion length was thus set to $1.5\sqrt{Dt}$ which corresponds to an amplitude reduction of 29%. Note that the role of triple junctions are neglected here, so the model will calculate a lower bond of $f_{gb}$.

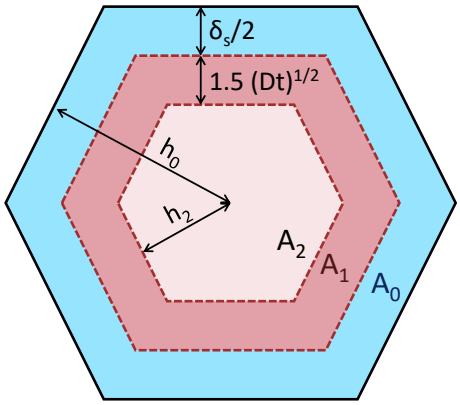


Figure A.10: Schematic representation of the diffusion in the vicinity of a prismatic GB.

Since the problem is two-dimensional, the volume fraction is reduced to an area fraction :

$$1 - f_{gb} = \frac{A_2}{A_0} \tag{A.1}$$

We can express $A_0$ and $A_2$ as a function of geometric parameters. Since the grain size $g_s$ was measured as the diameter of a disk with equivalent surface area, $A_0$ can be linked to both $h_0$ and $g_s$:

$$A_0 = \frac{\pi}{4}{g_s}^2 = 2\sqrt{3}{h_0}^2 \tag{A.2}$$

$$A_2 = 2\sqrt{3}{h_2}^2 \tag{A.3}$$

$$h_2 = h_0 - \frac{\delta_s + 3\sqrt{Dt}}{2} \tag{A.4}$$

By combining equations A.2, A.3 and A.4, we obtain:

$$\frac{A_2}{A_0} = \left(1 - \frac{\delta_s + 3\sqrt{Dt}}{2\,a\,g_s}\right)^2 \tag{A.5}$$

with $\delta_s$ the segregation width of the GB, $D$ the interdiffusion coefficient, $t$ the annealing time, $g_s$ the average grain size and $a = \sqrt{\frac{\pi}{8\sqrt{3}}} \simeq 0.476$ a geometric parameter.

## Appendix B. Test of APT global method

A set of simulations was carried out in order to test the APT global method. The simulation consists of a 2D box where the Cr concentration follows a sine wave in the y-direction. Additionally, two columnar GBs spreading in the y-direction are added, separated by 15 nm. The perturbation in concentration caused by the presence of the GB is simulated by a scaled normal distribution. The center of the GB is set at the average concentration of the box and the concentration far from the GB is set at the concentration of the sine wave at the corresponding y-coordinate. This normal distribution is characterized by its standard deviation $\sigma$, which acts a characteristic length scale. A random noise is then added to reproduce the statistics of APT data. The simulation boxes with concentration modulation amplitudes of 5, 7, 9 and 11 at.% and standard deviations of 0.2, 1 and 3 nm associated with their corresponding distributions and fits are given in Fig. B.11.

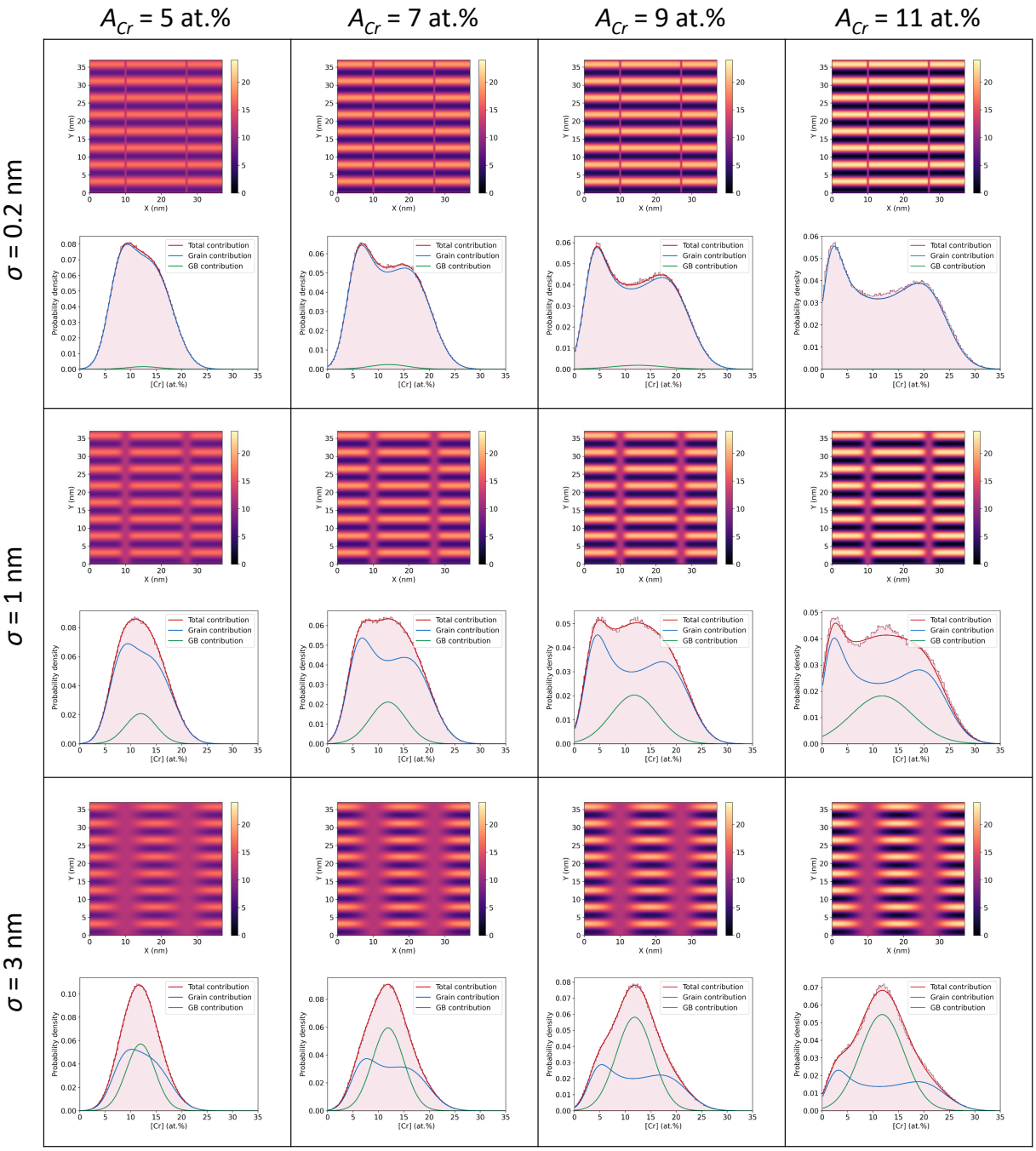


Figure B.11: 2D simulation boxes with concentration modulation amplitudes of 5, 7, 9 and 11 at.% and standard deviations $\sigma$ (characteristic length scale of the GBs) of 0.2, 1 and 3 nm and corresponding Cr concentration distributions and fits.

As seen from Fig. B.11, the algorithm can fit the simulated distributions reasonably well. The error $\epsilon$ on the determination of the amplitude, defined as $\epsilon = (A_{true} - A_{fit})/A_{true}$ as a function of the GB length scale $\sigma$ is plotted in Fig. B.12a.

As the influence of GBs increases (increase of $\sigma$), the error on the amplitude determination increases.

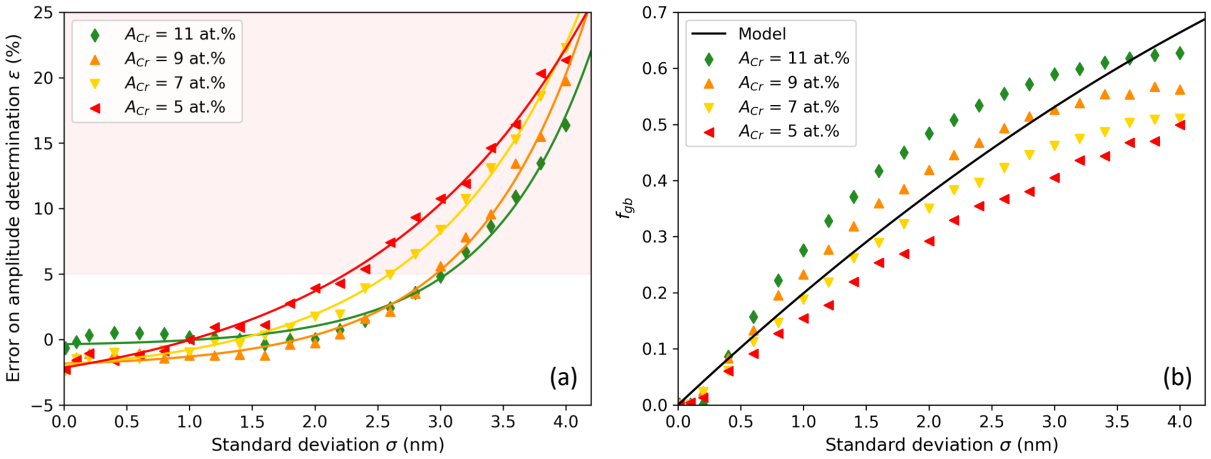


Figure B.12: (a) Impact of the true Cr amplitude and GB length scale $\sigma$ on the amplitude determination error $\epsilon = \left(A_{true} - A_{fit}\right)/A_{true}$ with the APT global method. (b) Impact of the true Cr amplitude and GB length scale $\sigma$ on the volume fraction of GB $f_{gb}$ determined by the APT global method. The evolution of $f_{gb}$ predicted by the model developed in Appendix A is also shown (black stright line). The simulation shows that the model produces negligible measurement errors for $f_{gb} \leq 0.5$.

This behavior is expected given that the diffusion fields from two adjacent boundaries start to overlap at a certain point and the true amplitude (representative of the boundary-free behavior) can not be retrieved. Another behavior that can be observed it that, as a global trend, the error is systematically superior for lower amplitudes. This behavior is also expected, given that the noise-to-signal ratio becomes significantly higher at lower amplitudes. The fitted grain-boundary fraction $f_{gb}$ (eq. 2) is always very close to the one determined with the model developed in Appendix A (Fig. B.12), which demonstrates a compatibility of both approaches. As a conclusion, the simulation shows that the model produces negligible errors for $f_{gb} \leq 0.5$.

## References


[1] C. Desgranges, F. Lequien, E. Aublant, M. Nastar, D. Monceau, Depletion and Voids Formation in the Substrate During High Temperature Oxidation of Ni–Cr Alloys, Oxidation of Metals 79 (2013) 93–105. doi:10.1007/s11085-012-9328-0.

[2] G. Laplanche, S. Berglund, C. Reinhart, A. Kostka, F. Fox, E. George, Phase stability and kinetics of $\sigma$-phase precipitation in CrMnFeCoNi high-entropy alloys, Acta Materialia 161 (2018) 338–351. doi:10.1016/j.actamat.2018.09.040.

[3] X. Li, N. Saunders, A. P. Miodownik, The coarsening kinetics of $\gamma'$ particles in nickel-based alloys, Metallurgical and Materials Transactions A 33 (2002) 3367–3373.

[4] J. DuMond, J. P. Youtz, An X-Ray Method of Determining Rates of Diffusion in the Solid State, Journal of Applied Physics 11 (1940) 357–365. doi:10.1063/1.1712784.

[5] J. W. Cahn, J. E. Hilliard, Free Energy of a Nonuniform System. I. Interfacial Free Energy, The Journal of Chemical Physics 28 (1958) 258–267. doi:10.1063/1.1744102.

[6] J. W. Cahn, On spinodal decomposition, Acta Metallurgica 9 (1961) 795–801. doi:https://doi.org/10.1016/0001-6160(61)90182-1.

[7] J. W. Cahn, Phase Separation by Spinodal Decomposition in Isotropic Systems, The Journal of Chemical Physics 42 (1965) 93–99. doi:10.1063/1.1695731.

[8] M. Nastar, Atomic diffusion theory challenging the Cahn-Hilliard method, Phys. Rev. B 90 (2014) 144101. doi:https://doi.org/10.1103/PhysRevB.90.144101.

[9] T. Südkamp, H. Bracht, Self-diffusion in crystalline silicon: A single diffusion activation enthalpy down to 755 ° C, Phys. Rev. B 94 (2016) 125208. doi:https://doi.org/10.1103/PhysRevB.94.125208.

[10] H. E. Cook, J. E. Hilliard, Effect of Gradient Energy on Diffusion in Gold-Silver Alloys, Journal of Applied Physics 40 (1969) 2191–2198. doi:10.1063/1.1657957.

[11] E. M. Philofsky, J. E. Hilliard, Effect of Coherency Strains on Diffusion in Copper-Palladium Alloys, Journal of Applied Physics 40 (1969) 2198–2205. doi:10.1063/1.1657958.

[12] P. C. McIntyre, D. T. Wu, M. Nastasi, Interdiffusion in epitaxial Co/Pt multilayers, Journal of Applied Physics 81 (1997) 637–645. doi:10.1063/1.364221.

[13] N. Zotov, J. Feydt, A. Savan, A. Ludwig, Interdiffusion in Fe–Pt multilayers, Journal of Applied Physics 100 (2006) 073517. doi:10.1063/1.2355552.

[14] P. Camilos, Atomic-scale modelling of diffusion in concentrated alloys, PhD thesis, Université Paris-Saclay, 2022.

[15] M. Murakami, D. D. Fontaine, J. M. Sanchez, J. Fodor, Ternary diffusion in multilayer Ag-Au-Cu thin films, Thin Solid Films 25 (1975) 465–482. doi:https://doi.org/10.1016/0040-6090(75)90065-6.

[16] C. V. Thompson, Structure Evolution During Processing of Polycrystalline Films, Annual Review of Materials Science 30 (2000) 159–190. doi:10.1146/annurev.matsci.30.1.159.

[17] H. Mehrer, High-diffusivity paths in metals, in: Diffusion in Solids, Springer Berlin, 2007.

[18] A. Debelle, A. Michel, M. Loyer-Prost, T. Rieger, A. Billard, M. Nastar, Determination of the interdiffusion coefficient at low temperature in Ni/NiCr nanometer-scale multilayers using X-ray reflectivity, Materialia 25 (2022) 101528. doi:10.1016/j.mtla.2022.101528.

[19] A. Debelle, A. Michel, M. Loyer-Prost, T. Rieger, A. Billard, M. Nastar, Corrigendum to 'Determination of the interdiffusion coefficient at low temperature in Ni/NiCr nanometer-scale multilayers using X-ray reflectivity' Materialia 25 (2022) 101528, Materialia 26 (2022) 101606. doi:10.1016/j.mtla.2022.101606.

[20] N. Zotov, A. Ludwig, Atomic mechanisms of interdiffusion in metallic multilayers, Materials Science and Engineering: C 27 (2007) 1470–1474. doi:10.1016/j.msec.2006.06.002.

[21] B. Gault, M. P. Moody, J. M. Cairney, S. P. Ringer, Analysis techniques for atom probe tomography, in: Atom Probe Microscopy, Springer New York, 2012.

[22] A. L. Greer, Measurements of atomic diffusion using metallic multilayers, Current Opinion in Solid State and Materials Science 2 (1997) 300–304. doi:10.1016/S1359-0286(97)80119-2.

[23] A. Greer, N. Karpe, J. Bøttiger, Diffusional aspects of the solid state amorphization reaction, Journal of Alloys and Compounds 194 (1993) 199–211. doi:10.1016/0925-8388(93)90003-6.

[24] J. Růžičková, B. Million, Self-diffusion of the components in the F.C.C. phase of binary solid solutions of the Fe-Ni-Cr system, Materials Science and Engineering 50 (1981) 59–64. doi:10.1016/0025-5416(81)90086-0.

[25] P. Nash, The Cr-Ni (Chromium-Nickel) system, Bulletin of Alloy Phase Diagrams 7 (1986) 466–476.

[26] R. W. Balluffi, Grain boundary diffusion mechanisms in metals, Metallurgical transactions B (1982) 27.

[27] D. Turnbull, R. Hoffman, The effect of relative crystal and boundary orientations on grain boundary diffusion rates, Acta Metallurgica 2 (1954) 419–426. doi:10.1016/0001-6160(54)90061-9.

[28] S. V. Divinski, L. N. Larikov, On the Diffusion Anisotropy of Polycrystals, Cryst. Res. Technol. 30 (1995) 957–962. doi:10.1002/crat.2170300715.

[29] I. Herbeuval, M. Biscondi, C. Goux, Effect of Intercrystalline Structure on the Diffusion of Zinc in Boundaries Between Aluminum Crystals of Symmetrical Structure, Mem Sci Rev Metal 70 (1973) 39 – 46.

[30] T. Surholt, D. Molodov, C. Herzig, Orientation dependence of Ge diffusion along symmetrical [111] tilt grain boundaries in Al, Acta Materialia 46 (1998) 5345–5355. doi:10.1016/S1359-6454(98)00237-7.

[31] T. Gheno, F. Jomard, C. Desgranges, L. Martinelli, Grain boundary diffusion of chromium in polycrystalline nickel studied by SIMS, Materialia 6 (2019) 100283. doi:10.1016/j.mtla.2019.100283.

[32] P. Moulin, A. Huntz, P. Lacombe, Influence du carbone sur la diffusion du chrome et du nickel en volume et dans les joints de grains de l'alliage Ni-Cr 80/20, Acta Metallurgica 27 (1979) 1431–1443. doi:10.1016/0001-6160(79)90165-2.

[33] J. Čermák, Grain boundary self-diffusion of 51Cr and 59Fe in austenitic Ni-Fe-Cr alloys, Materials Science and Engineering: A 148 (1991) 279–287. doi:10.1016/0921-5093(91)90830-G.
[34] T.-F. Chen, G. Tiwari, Y. Iijima, K. Yamauchi, Volume and Grain Boundary Diffusion of Chromium in Ni-Base Ni-Cr-Fe Alloys, Mater. Trans. 44 (2003) 40–46. doi:10.2320/matertrans.44.40.
[35] S. V. Divinski, G. Reglitz, G. Wilde, Grain boundary self-diffusion in polycrystalline nickel of different purity levels, Acta Materialia 58 (2010) 386–395. doi:10.1016/j.actamat.2009.09.015.
[36] M. R. Chellali, Z. Balogh, H. Bouchikhaoui, R. Schlesiger, P. Stender, L. Zheng, G. Schmitz, Triple Junction Transport and the Impact of Grain Boundary Width in Nanocrystalline Cu, Nano Lett. 12 (2012) 3448–3454. doi:10.1021/nl300751q.
[37] C. Herzig, S. V. Divinski, Grain Boundary Diffusion in Metals: Recent Developments, Mater. Trans. 44 (2003) 14–27. doi:10.2320/matertrans.44.14.
[38] M. K. Miller, M. G. Hetherington, Local magnification effects in the atom probe, Surface Science 246 (1991) 442–449. doi:https://doi.org/10.1016/0039-6028(91)90449-3.
[39] X. Sauvage, L. Renaud, B. Deconihout, D. Blavette, D. H. Ping, K. Hono, Solid state amorphization in cold drawn Cu/Nb wires, Acta Materialia 49 (2001) 389–394. doi:https://doi.org/10.1016/S1359-6454(00)00338-4.
[40] Z. Peng, T. Meiners, Y. Lu, C. H. Liebscher, A. Kostka, D. Raabe, B. Gault, Quantitative analysis of grain boundary diffusion, segregation and precipitation at a sub-nanometer scale, Acta Materialia 225 (2022) 117522. doi:10.1016/j.actamat.2021.117522.
[41] N. Choi, S. Taheriniya, S. Yang, V. A. Esin, J. H. Yu, J.-S. Lee, G. Wilde, S. V. Divinski, "Non-equilibrium" grain boundaries in additively manufactured CoCrFeMnNi high-entropy alloy: Enhanced diffusion and strong segregation, Journal of Applied Physics 132 (2022) 245105. doi:10.1063/5.0133144.
[42] J. Startt, R. Dingreville, S. Raiman, C. Deo, An electronic origin to the oscillatory segregation behavior in Ni-Cr and other BCC defects in FCC metals, Acta Materialia 218 (2021) 117215. doi:https://doi.org/10.1016/j.actamat.2021.117215.
[43] L. G. Harrison, Influence of dislocations on diffusion kinetics in solids with particular reference to the alkali halides, Transactions of the Faraday Society 57 (1961) 1191. doi:10.1039/tf9615701191.
[44] A. Glaeser, J. Evans, Effect of grain boundary migration on apparent boundary diffusion coefficients, Acta Metallurgica 34 (1986) 1545–1552. doi:10.1016/0001-6160(86)90099-4.
[45] H. P. Longworth, C. V. Thompson, Abnormal grain growth in aluminum alloy thin films, Journal of Applied Physics 69 (1991) 3929–3940. doi:10.1063/1.348452.
[46] S. Du, Y. Li, Effect of Annealing on Microstructure and Mechanical Properties of Magnetron Sputtered Cu Thin Films, Advances in Materials Science and Engineering 2015 (2015) 1–8. doi:10.1155/2015/969580.
[47] C. M. Barr, S. M. Foiles, M. Alkayyali, Y. Mahmood, P. M. Price, D. P. Adams, B. L. Boyce, F. Abdeljawad, K. Hattar, The role of grain boundary character in solute segregation and thermal stability of nanocrystalline Pt–Au, Nanoscale 13 (2021) 3552–3563. doi:10.1039/D0NR07180C.
[48] N. Moelans, B. Blanpain, P. Wollants, Pinning effect of second-phase particles on grain growth in polycrystalline films studied by 3-D phase field simulations, Acta Materialia 55 (2007) 2173–2182. doi:10.1016/j.actamat.2006.11.018.
[49] S. Perusin, D. Monceau, E. Andrieu, Investigations on the Diffusion of Oxygen in Nickel at 1000 ° C by SIMS Analysis, Journal of The Electrochemical Society 152 (2005) E390. doi:https://doi.org/10.1149/1.2116787.
[50] J. D. Poplawsky, R. Pillai, Q.-Q. Ren, A. J. Breen, B. Gault, M. P. Brady, Measuring oxygen solubility in Ni grains and boundaries after oxidation using atom probe tomography, Scripta Materialia 210 (2022) 114411. doi:https://doi.org/10.1016/j.scriptamat.2021.114411.
[51] S. Rajeshwari K., S. Sankaran, K. Hari Kumar, H. Rösner, M. Peterlechner, V. A. Esin, S. Divinski, G. Wilde, Grain boundary diffusion and grain boundary structures of a Ni-Cr-Fe- alloy: Evidences for grain boundary phase transitions, Acta Materialia 195 (2020) 501–518. doi:10.1016/j.actamat.2020.05.051.
[52] M. Hillert, Solute drag in grain boundary migration and phase transformations, Acta Materialia 52 (2004) 5289–5293. doi:https://doi.org/10.1016/j.actamat.2004.07.032.
[53] S. G. Kim, Y. B. Park, Grain boundary segregation, solute drag and abnormal grain growth, Acta Materialia 56 (2008) 3739–3753. doi:https://doi.org/10.1016/j.actamat.2008.04.007.
[54] S. J. Dillon, M. Tang, W. C. Carter, M. P. Harmer, Complexion: A new concept for kinetic engineering in materials science, Acta Materialia 55 (2007) 6208–6218. doi:10.1016/j.actamat.2007.07.029.
[55] P. R. Cantwell, M. Tang, S. J. Dillon, J. Luo, G. S. Rohrer, M. P. Harmer, Grain boundary complexions, Acta Materialia 62 (2014) 1–48. doi:10.1016/j.actamat.2013.07.037.
[56] P. R. Cantwell, T. Frolov, T. J. Rupert, A. R. Krause, C. J. Marvel, G. S. Rohrer, J. M. Rickman, M. P. Harmer, Grain Boundary Complexion Transitions, Annu. Rev. Mater. Res. 50 (2020) 465–492. doi:10.1146/annurev-matsci-081619-114055.
[57] E. W. Hart, On the role of dislocations in bulk diffusion, Acta Metallurgica 5 (1957) 597. doi:https://doi.org/10.1016/0001-6160(57)90127-X.
[58] H. Nakajima, H. Fujimori, M. Koiwa, Interdiffusion and structural relaxation in Mo/Si multilayer films, Journal of Applied Physics 63 (1988) 1046–1051. doi:https://doi.org/10.1063/1.340005.
[59] I. Hashim, H. A. Atwater, K. T. Y. Kung, R. M. Valletta, Evolution of structural and magnetic properties in Ta/Ni $_{81}$Fe $_{19}$ multilayer thin films, Journal of Applied Physics 74 (1993) 458–464. doi:10.1063/1.355252.
[60] B. Yao, K. R. Coffey, The effective interdiffusivity, structure, and magnetic properties of Fe/Pt in multilayer films, Journal of Applied Physics 103 (2008) 07E107. doi:10.1063/1.2828978.
[61] F. Vurpillot, D. Larson, A. Cerezo, Improvement of multilayer analyses with a three-dimensional atom probe, Surface and Interface Analysis 36 (2004) 552–558. doi:10.1002/sia.1697.
[62] E. A. Marquis, B. P. Geiser, T. J. Prosa, D. J. Larson, Evolution of tip shape during field evaporation of complex multilayer structures, Journal of Microscopy 241 (2011) 225–233. doi:10.1111/j.1365-2818.2010.03421.x.

[63] R. Venos, W. Pamler, H. Hoffmann, Grain boundary diffusion in Ni-Cu multilayer films, Thin Solid Films 162 (1988) 155–160. doi:10.1016/0040-6090(88)90203-9.